2024 IEEE/RSJ International Conference on Intelligent Robots and Systems (IROS)
October 14-18, 2024. Abu Dhabi, UAE

Hardware-Based Time Synchronization for a Multi-Sensor System

Yueqi Wang†, Tangyou Liu†, Licheng Feng, Jinze Wang, Yang Yang, Jianjun Bao, Binghao Li*, *Senior Member, IEEE*, and Liao Wu*, *Member, IEEE*

***Abstract*— Accurate time synchronization is crucial for multi-sensor fusion, which is widely used in mobile robotics, autonomous driving, and virtual reality. Despite many advancements, precise multi-sensor synchronization is still challenging due to the sensors' internal characteristics, data filtering, disjointed clock reference, and transmission delay caused by operation system scheduling. This paper proposes a novel hardware-based synchronization solution to achieve synchronization in microsecond-level precision. By introducing a Sensor Adaptor board that provides a unified clock reference, the proposed hardware architecture enables high-precision synchronization across multiple sensors. Furthermore, we develop a method for Visual-Inertial time synchronization that actively controls the exposure duration using an ambient light sensor. By managing the IMU clock signal and exposure trigger, we align the camera's sampling moment with the authentic IMU sampling time and significantly reduce the time discrepancy in the Visual-Inertial system. Experiments are conducted to evaluate the efficiency of the proposed method and system, including comparisons with previous work. The results indicate that our method can achieve precise time synchronization and be successfully implemented in multi-sensor systems.**

I. INTRODUCTION

Data fusion from multiple sensors, such as cameras, inertial measurement units (IMUs), and light detection and ranging (LiDAR) sensors, is widely used in diverse fields, including mobile robotics, autonomous driving, and virtual reality [1]–[3]. Most data fusion methods require accurately aligning the timestamps of all the measurements to a single clock. Consequently, high-precision time synchronization is crucial for effective data fusion in multi-sensor systems.

Various approaches have been proposed for time synchronization and can be generally categorized into two groups. The first group assumes that the time offsets between sensors' clock systems are stable and constant [4]. Based on this assumption, it is possible to develop a framework of temporal calibration algorithms to reduce or eliminate data synchronization errors among multiple sensors [5].

This research was supported under the Australian Research Council's Industrial Transformation Research Hub Programme (IH210100048).
*Corresponding authors: Binghao Li (*binghao.li@unsw.edu.au*) and Liao Wu (*liao.wu@unsw.edu.au*). †Yueqi Wang and Tangyou Liu contributed equally to this paper.

Yueqi Wang, Tangyou Liu, Yang Yang, and Liao Wu are with the School of Mechanical & Manufacturing Engineering, University of New South Wales, Sydney, Australia.

Licheng Feng and Binghao Li are with the School of Minerals and Energy Resources Engineering, University of New South Wales, Sydney, Australia.

Jinze Wang is with Swinburne University of Technology, Melbourne, Australia.

Jianjun Bao is with Changzhou Institute Co., Ltd of CCTEG, State Key Laboratory of Intelligent Coal Mining and Strata Control, and Tiandi (Changzhou) Automation Co., Ltd, Changzhou, China.

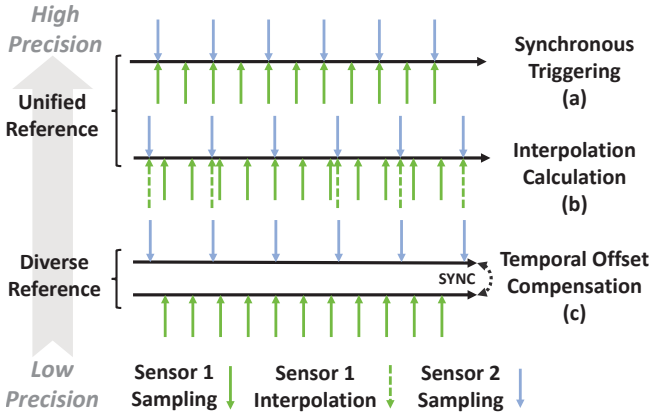

Fig. 1: Classifications of hardware-based time synchronization methods in the multi-sensor system.

For example, a representative offline calibration algorithm, Kalibr, was designed to optimize batch continuous-time estimation for determining fixed time offsets in Visual-Inertial synchronization systems [6]–[8]. Online calibration methods, such as that presented in [9], were also proposed to estimate the fixed time offsets through nonlinear optimization.

The second group, however, challenges the validity of the constant-time-offset assumption [10]. In practical applications, the hardware clock systems may be unstable, resulting in dynamic shifts in the time discrepancies among sensors. When calibration-based algorithms are applied to these systems, the fixed time offset generated from these algorithms will struggle to realize fine synchronization at each measurement. To cope with clock systems' dynamic shifts, methods in this group propose addressing time synchronization at the hardware level for applications requiring high-precision data fusion.

As shown in Fig. 1, hardware-based time synchronization can be classified into two categories with three types according to the sources of clock references and sampling methods, and the precision of the types increases with the elevation of the arrow. For a multi-sensor system with diverse clock references shown in Fig. 1(c), it is crucial to compensate for the temporal offset between their respective clock references before finer alignments are applied. A common approach to synchronizing between multiple clocks is to run an NTP (Network Time Protocol) [11] server on one device and adjust others to it. However, the method may suffer from significant latency [12]. Improved techniques such as TICSync [13] have been developed to increase efficiency, but fluctuations in calculating the offset values between references still exist, compromising the accuracy

and reliability of the synchronization.

For the second category of hardware-based synchronization, the multi-sensor system is sampled against a unified clock reference. Based on sampling rates and triggering availability, these systems can be further divided into two types: systems using interpolation calculation and systems using synchronous triggering. As demonstrated in Fig. 1(b), when the sensors' output frequency lacks integer multiple relationships, time synchronization requires interpolation to obtain all the measurements at the same timestamps. For example, in Visual-Inertial systems [14], [15], fitting a curve through discrete points is often employed to calculate more accurate interpolated values.

Higher accuracy can be achieved if the sensors can be genuinely sampled at the same timestamps as shown in Fig. 1(a), which requires a unique hardware design to enable synchronous triggering between multiple sensors. To this end, efforts have been put into novel hardware design to enable simultaneous signal triggering in LiDAR-Visual [16], [17] and Visual-Inertial [18] synchronization systems. However, while these systems have shown significant improvement in accuracy, their design is often sensor-specific and limited to synchronization between sensor pairs. When new sensors are introduced, the systems still face the challenge of time synchronization between different clock references. A more adaptive architecture that can accommodate more sensors' synchronization is much needed.

Therefore, this paper's first contribution is proposing a new hardware architecture that enables the synchronization of three or more sensors under a unified clock reference and validating its performance in a system that includes LiDAR, visual, and IMU sensors.

In addition, during our implementation of the hardware architecture, we found that the synchronization accuracy between the visual and IMU sensors could be further improved over the state-of-the-art [18]. Traditional hardware-based Visual-Inertial synchronization often uses the start moment of the camera's strobe as its sampling timestamp, overlooking the time needed for exposure. In [18], a pre-exposure method was proposed to predict the camera's genuine sampling moments, compensating for the exposure-induced delay in visual sensors. However, this method overlooked that the inertial sensor's uncontrollable sampling moments could also introduce delays in the simultaneous triggering mechanism.

Hence, this paper's second contribution is presenting a hardware-based Visual-Inertial synchronization method that enables genuine simultaneous sampling between the camera and the IMU with the assistance of an ambient light detector and careful accounting for the IMU's delay.

II. HARDWARE SYSTEM

To achieve precise synchronization between multiple sensors, we propose a hardware architecture by introducing a mid-layer between sensors and the computation device. This mid-layer is responsible for all time synchronization and calibration tasks so that the computation device can focus on processing data and algorithms. Details of this architecture are presented in Section III-A.

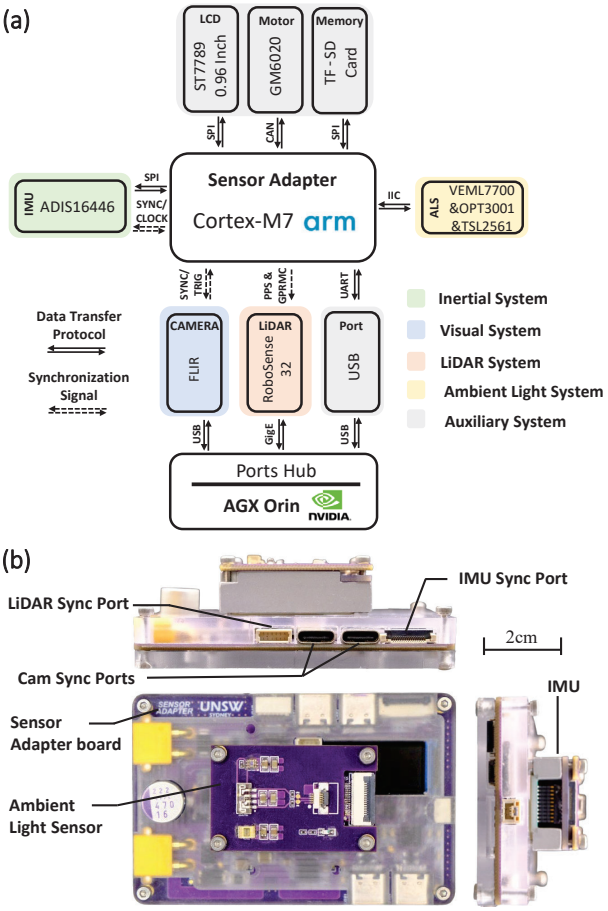

Fig. 2: (a) Hardware structure of the multi-sensor platform. (b) A customized unit prototype, which adopts a multi-component layered design strategy, stacking the ambient light sensor, IMU, acrylic cases, and Sensor Adapter together layer by layer, and provides power distribution, data transmission, and time synchronization functions through hardware interfaces to sensors.

To verify the feasibility of the proposed hardware architecture, we develop a multi-sensor platform, as shown in Fig. 2. The platform comprises an edge computing center (Jetson Orin, NVIDIA, US), an inertial measurement unit (ADIS16446, Analog Devices, US), an industrial camera (FLIR, US), a LiDAR (Robosense-32, Robosense, China), a customized ambient light sensor, and a Sensor Adapter. The Sensor Adapter operates as the time synchronization core unit for the entire system and enables synchronization among all the sensors under a unified clock reference.

As the core component in the multi-sensor system shown in Fig. 2, the Sensor Adapter based on a 32-bit microcontroller of the Cortex-M7 core supports a high peripheral frequency, which could be sped up to 400MHz by multiplying the external crystal oscillator through the phase-locked loop. In addition, external sensors and hardware interfaces can be classified into five subsystems:

1) Visual Subsystem: The multi-sensor platform offers two camera extension ports. Cameras can be selected according to the low-light sensitivity, global shutter, and external triggering functionality to satisfy the requirements of hardware-based synchronization. Through hardware interfaces, BFLY-U3-03S2 (FLIR, US) offers high-quality imaging, digital trigger input, and strobe signal output.
2) Inertial Subsystem: The current prototype allows two connection ports for the IMU subsystem, supporting various types of IMUs. By default, each Sensor Adapter is fitted with a MEMS IMU (Analog Devices, US) from the ADIS series. The ADIS16505, ADIS16446, and ADIS16488 are equipped with higher-quality calibrated gyroscopes and accelerometers. Primarily, they provide GPIO ports for external sync clock input and data-ready signal output.
3) LiDAR Subsystem: The Sensor Adapter provides power supply, over-voltage, and over-current circuit protection for the LiDAR. It supports various models of LiDAR like Robosense-32, Livox Mid360, Hesai Pandar64, etc.
4) Ambient Light Subsystem: The Sensor Adapter board is topped with a customized ambient light detection board for environmental light evaluation shown in Fig. 2, which assembles three ambient light sensors: TSL2561 (TAOS, US), VEML7700 (VISHAY, US), and OPT3001 (TI, US) for the noisy filter, rapid response and data fusion.
5) Auxiliary Subsystem: This subsystem is charged for system debugging, data storage, and transfer tasks between the Sensor Adapter and the AGX Orin platform.

III. HARDWARE-BASED TIME SYNCHRONIZATION

A. Synchronization for a Unified Clock Reference

Regarding hardware-based unified clock reference for multi-sensor synchronization, the current market lacks mature solutions or frameworks to overcome the time synchronization challenges across different platforms and sensors. Current systems can often only achieve time synchronization based on specific sensor pairings because they cannot simultaneously provide a unified clock source and extended time mechanism for newly added sensors. To enhance the scalability, Osadcuks *et al.* [17] introduced a customized board to integrate sensors and computing platforms, thereby adapting to various synchronization mechanisms. However, their system time still relied on external input signals from LiDAR as the primary clock source, which can lead to timing disruptions due to disturbances from the input signals.

We propose a new hardware architecture here to sample various types of sensors, including LiDAR, visual, and inertial sensors (LVI), in one system under a unified clock reference. The architecture utilizes the Sensor Adapter as a 'buffer layer' to interface sensors according to their synchronization properties. It allows the computing center to focus on data receiving and subsequent algorithm applications, as shown in Fig. 2.

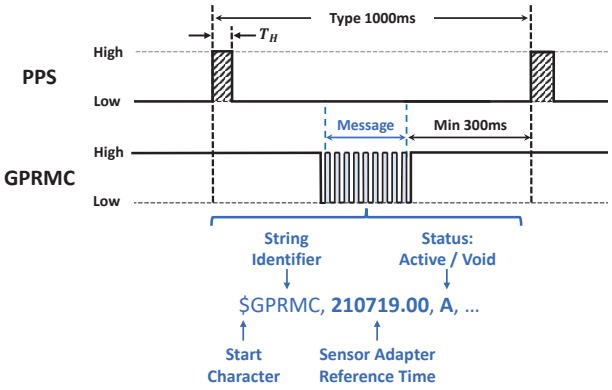

Fig. 3: The data timing of Pulse-Per-second (PPS) signal and GPRMC messages' data format

In the time synchronization process for the unified clock reference, sensors in the LVI system synchronize with the Sensor Adapter according to their respective system characteristics. For visual sensors, external signals can trigger sampling, and generated pixel data do not include timestamp information. By leveraging this feature, we use the Sensor Adapter to generate a periodic 25Hz trigger signal for cameras and record timestamps of the signal generation in the local clock as the preliminary occurrence time of images.

Then, for IMUs that enable generating sampling completion signals or sending data at a fixed frequency, the Sensor Adapter communicates with the IMU through the hardware chip-level protocol, such as serial peripheral interface (SPI). Using the Sensor Adapter to record arrival moments of sampling completion signals under the local clock, the IMU could synchronize time with other sensors in the unified clock reference.

For the LiDAR sensor with a complex timing mechanism, its point-cloud data includes timestamp messages generated from its internal clock system. We use the Sensor Adapter to simulate the pulse-per-second signal (PPS) and global positioning recommended minimum signal (GPRMC) generated from the global navigation satellite system (GNSS) modules [19] to align the internal clock of the LiDAR with the local clock from Sensor Adapter. Consequently, the point-cloud data generated from the LiDAR can be aligned with a Visual-Inertial system under a unified clock reference, i.e., the Sensor Adapter's local clock.

As shown in Fig. 3, the simulated PPS signal is generated every 1000ms and lasts at a high level T_H for 5ms to 100ms. Following each PPS signal transmission, the simulated GPRMC messages are forwarded to LiDAR, which contains the Sensor Adapter's local clock time message in coordinated universal time (UTC) format corresponding to the PPS signal's rising moment. The simulated GPRMC message only incorporates imperative identifiers and timestamps from the Sensor Adapter's local clock time, denoting the start of the PPS signal pulse. To cooperate with PPS & GPRMC signals for synchronizing the timestamps included in the point-cloud messages, the LiDAR internal clock system will automatically update the timer value according to the

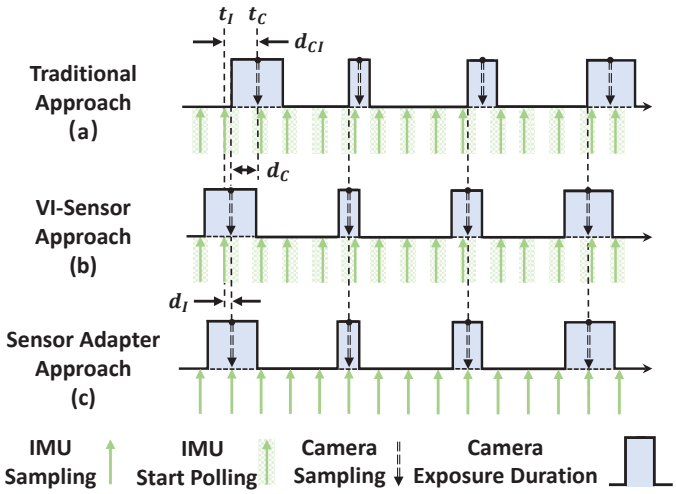

Fig. 4: Three synchronization approaches for Visual-Inertial system. (a) Traditional approach, where d_{CI} is the deviation between true sampling moments of camera and IMU. $d_{CI} = d_C + d_I$, wherein d_C and d_I are deviations resulting from camera exposure and IMU polling, respectively. (b) VI-Sensor approach [18], where d_C has been considered. (c) Our Sensor Adapter approach, where both d_C and d_I have been eliminated.

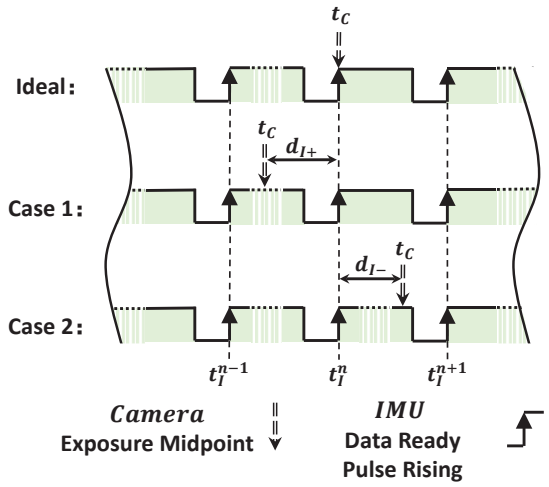

Fig. 5: The ideal condition and two cases of IMU-Camera deviation that corresponds to Fig. 4(c). Deviations d_{I+}^n and d_{I-}^n of two cases equal to $t_I^n - t_C$. t_I^n is the n-th authentic IMU sampling moment, and t_C is the corresponding camera exposure midpoint.

GPRMC message at the rising edge of the PPS arriving.

By simulating the PPS & GPRMC signals and replacing the LiDAR's internal system clock with the Sensor Adapter local time, the system can ensure that the timestamps contained in the returned point-cloud data are referring to the same clock with other visual and inertial sensors.

B. Visual-Inertial System Synchronization

For easier understanding and without loss of generality, the following description focuses on one synchronization loop.

1) The traditional and VI-Sensor approaches: Referring to the hardware-based synchronization classifications in Fig. 1(a), accuracy can be further improved if sensors can sample at the same timestamp after constructing a unified time reference into the system. However, for a pair of sensors like a Visual-Inertial system, it is hard to align their true sampling moments if the sensors' inherent characteristics are not taken into account. As illustrated in Fig. 4(a), the traditional approach for simultaneously triggering the Visual-Inertial system is periodically starting camera exposure and sending IMU data-reading requests through chip communication protocols. In this method, there is a deviation d_{CI} between the timestamp of the camera's real sampling moment t_C and the timestamp of the IMU's real sampling moment t_I. This deviation d_{CI} can be further divided into the deviation d_C caused by camera exposure [7] and deviation d_I caused by IMU, i.e.,

$$t_I = t_C + d_{CI} = t_C + (d_C + d_I)\,. \tag{1}$$

Aiming to eliminate the exposure deviation d_C existing in the traditional approach, VI-Sensor [18] suggested that the genuine sampling moment for visual sensors should be timestamped at the exposure midpoint. As shown in Fig. 4(b), they let the camera expose in advance and align the IMU polling request starting with the predicted exposure midpoint. This approach assumed the light condition remained unchanged between adjacent frames so that the exposure duration of the last exposure could be used to predict the current exposure midpoint. However, when the camera operates in auto exposure mode, the exposure duration varies with changes in ambient light intensity. As a result, there can be a significant error between the predicted and true exposure midpoints when the light condition fluctuates and d_C varies.

In addition, as shown in Fig. 4(a) and 4(b), the two previous methods identify the start of IMU polling as its actual sampling moment. However, the polling process merely initiates data reading from registers by using hardware protocols. Technically, the authentic sampling moment should be identified as the moment when the data sampling completion flag-bit is updated in the IMU registers or when IMU actively sends a data-ready signal to the Sensor Adapter. Therefore, the delay in the IMU sampling, d_I, needs to be compensated for as well to achieve authentic synchronization.

2) Sensor Adapter approach: To eliminate both deviations d_C in the visual sensor and d_I in IMU, we present a Sensor Adapter approach, as shown in Fig. 4(c). The camera exposure midpoint t_C is strictly aligned with the authentic IMU sampling moment t_I, which implies that the acquisition of IMU data is precisely synchronized with the camera sampling process. Compared to monitoring the flag-bit, detecting changes in the data-ready signal is more straightforward when using an external hardware interrupt. However, accurately predicting the exact moment of data-ready signal generation is challenging when the IMU operates in normal mode and publishes data at a fixed frequency. Consequently, if we do not predict or control the arrival of the IMU sampling moment, it becomes challenging to align

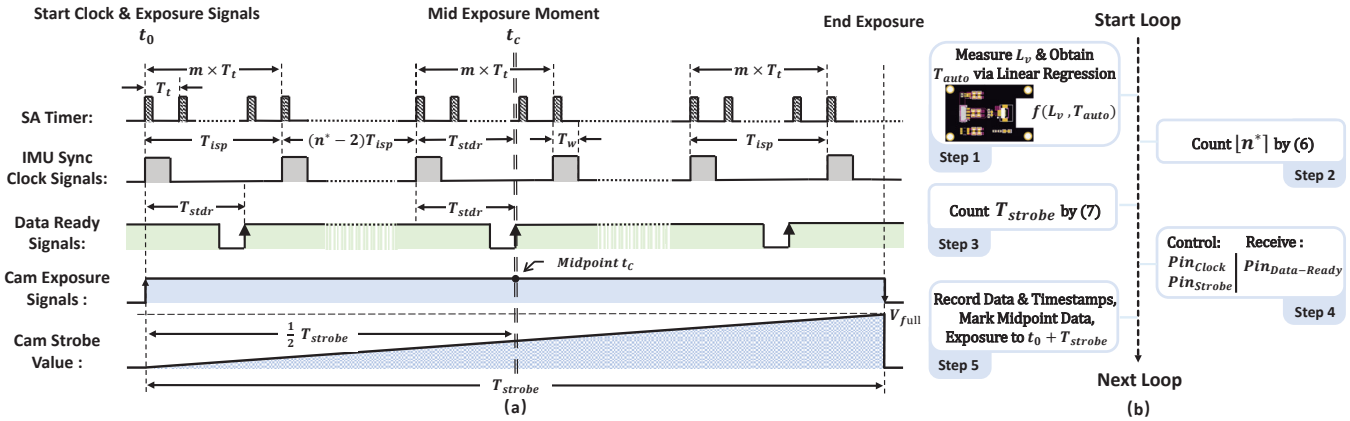

Fig. 6: (a) The process of one synchronization loop. t_I^n and t_C indicate the authentic IMU sampling moment and camera exposure midpoint, respectively. $n^* \in n$ is the index for aligning t_C. (b) Critical steps of one synchronization loop.

the exposure midpoint t_C with the authentic IMU sampling moment t_I. This misalignment results in a deviation d_I, which can be categorized into two cases: d_{I+} and d_{I-}, as shown in Fig. 5,

$$\begin{cases} d_{I+} = t_I^n - t_C, \, t_I^n > t_C \\ d_{I-} = t_I^n - t_C, \, t_I^n < t_C \end{cases}, \tag{2}$$

where t_I^n is the n-th authentic IMU sampling moment, t_C is the corresponding camera exposure midpoint, and $n \in \mathbb{N}^+$.

Therefore, to eliminate the deviation d_{CI} between exposure midpoint t_C and the authentic IMU sampling moment t_I, we must compensate for both d_C and d_I.

To eliminate d_C, we deploy a customized light sensor to capture the dynamic ambient light intensity. By collecting the light intensity L_v and its corresponding camera's exposure duration T_{auto} in automatic exposure mode, we can obtain their relationship and assume it can be formulated as

$$T_{auto} = f(L_v). \tag{3}$$

In turn, based on (3) and the current light intensity L_v, we can get the corresponding automatic exposure duration T_{auto}. Referring to this duration value, we can control the start and stop of the camera exposure actively, thereby controlling the occurrence of the exposure midpoint at the expected moment while avoiding overexposure and underexposure.

To eliminate d_I in (2), we actively supply an external sync clock signal to the IMU. Leveraging the timing mechanism between the external sync clock and the data-ready signal, we can indirectly control the timing of the rising edge of the IMU data-ready signal's occurrence. To ensure that the sampling of the IMU occurs precisely at the expected moment, we need to coordinate the SA's timer, external sync clock signal, camera exposure signal, and data-ready signal. According to the datasheet, in external sync clock input mode, we can control the sampling rate of the IMU by setting the period T_{isp} of the external sync clock signal, as depicted in Fig. 6(a). Upon receiving each external sync clock signal, the IMU finalizes data acquisition and emits a data-ready signal after a fixed duration T_{stdr}. Then, we can precisely obtain each authentic IMU sampling moment by

Parameter	Description	Value Min	Value Type	Value Max	Unit
T_{isp}	Input sync period	900			μs
T_{stdr}	Input sync to data ready transition		600		μs
T_{strobe}	Exposure duration	1.2			ms
T_t	Sensor Adapter timer		25		μs
T_w	Input sync positive pulse width		25		μs

TABLE I: Timing specifications in Fig. 6(a) for system synchronization are listed. T_{stdr} and T_w are fixed values set from datasheets.

$$t_I^n = t_0 + (n-1)\, T_{isp} + T_{stdr}\,, \tag{4}$$

where t_0 is the initial time of the VI synchronization loop. The values of the relevant parameters are also listed in Table I.

Generally, the sampling frequency of IMU f_I is much higher than that of the camera f_C. Therefore, we want to find the target index $n^* \in n$ and align exposure midpoint t_C with the n^*-th authentic IMU sampling moment $t_I^{n^*}$ s.t.

$$t_C = \frac{1}{2} T_{auto} + t_0 = t_I^{n^*}\,, \tag{5}$$

where T_{auto} is the camera exposure duration referring to (3). According to (5), we can formulate n^* as

$$n^* = \frac{\frac{1}{2} T_{auto} - T_{stdr} + T_{isp}}{T_{isp}}\,. \tag{6}$$

However, n^* in (6) is not always an integer that can be used to index authentic IMU sampling moment. Therefore, we need to optimize T_{auto}, and we define this optimized exposure duration as T_{strobe}. It can be formulated as

$$T_{strobe} = 2(\lfloor n^* \rceil - 1)\, T_{isp} + T_{stdr}\,, \tag{7}$$

where $\lfloor n^* \rceil$ is the round of n^*. With T_{strobe}, we can exactly align t_C with $t_I^{\lfloor n^* \rceil}$, i.e., eliminating the deviation d_{CI} in (1).

In one loop, the SA continuously provides the external sync clock signal to the IMU, records the timestamp at the exposure midpoint, and maintains the camera exposure signal until $t = t_0 + T_{strobe}$. For easy comprehension, we summarize the above synchronization process as Fig. 6(a), and its critical steps are shown in Fig. 6(b).

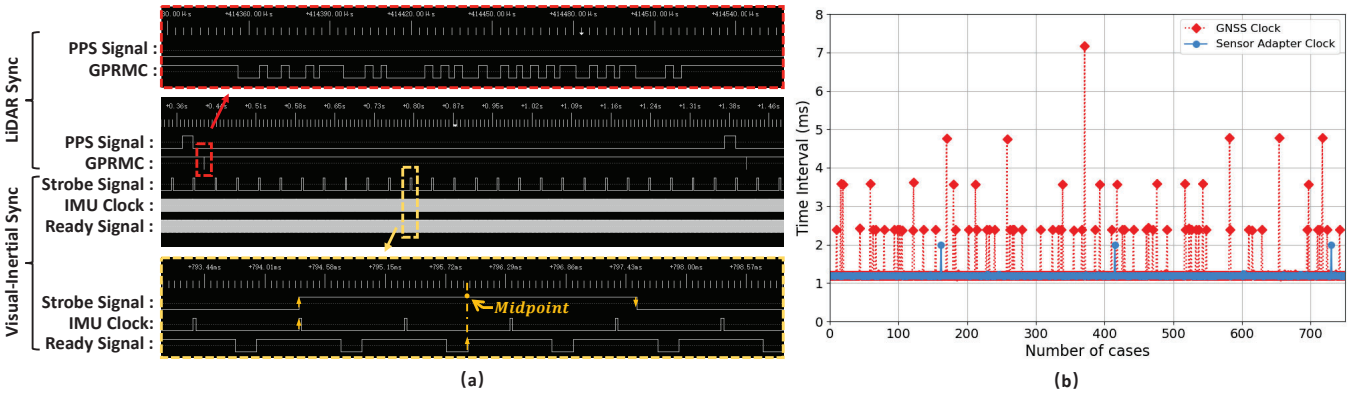

Fig. 7: (a) Time synchronization segment signals diagram captured by a logic-analyzer DSLogic (DreamSource, China). For LiDAR synchronization, the measured waveform matches the schematic shown in Fig. 3, the GPRMC message being emitted 20ms after the PPS rising edge. For Visual-Inertial synchronization, the captured timing diagram matches the expected outcome as set in Fig. 6(a), the IMU sampling completion moment and the midpoint of the camera exposure having an error of less than 0.001 ms. (b) Distribution of packets time intervals from different clock references.

Method	Standard Deviation [ms]	Average Value [ms]	Offset Calculation
Internal Clock	0.0695	0.1889	Required
GNSS Module	0.5380	1.3428	Required
Sensor Adapter	0.0856	0.1991	Not Required

TABLE II: Time interval results of three synchronization methods.

IV. Evaluation & Discussion

A. The unified clock reference evaluation

We first evaluated and discussed the performance of the customized multi-sensor system shown in Fig. 2. By sampling and measuring the synchronization signals emitted from the Sensor Adapter, we demonstrated that our LVI system could achieve data sampling and recording under the unified clock reference. Fig. 7(a) shows the related signals in one synchronization loop that is depicted in Fig. 6.

In addition, we evaluated the clock stability of LiDAR sensors by comparing the time interval values with different clock sources as the reference for data sampling:

1) Independent internal LiDAR clock;
2) Independent clock provided by the GNSS module;
3) Unified clock provided by the Sensor Adapter.

By running the system in indoor environments and providing the above different clock references for LiDAR, Robosense-32, we could measure the time intervals between timestamps of adjacent point-cloud data packets. The result is shown in Fig. 7(b). Then, we used statistical standard deviation and average value methods to analyze the time intervals, and the results are listed in Table II.

From Table II, we see the sensor relying on the GNSS module had the highest time interval standard deviation (0.0538ms), which indicates it suffered from fluctuation in the timestamping procedure. This could be because the module automatically switched to use the built-in oscillator as an alternative time source when the GNSS signal was lost or disrupted. This repeatedly switching process in GNSS-denied environments could lead timestamps to undergo abrupt changes and result in unfair data distribution. Moreover, the time intervals of the processes on the internal clock and the Sensor Adapter were similar (around 0.0103ms). This indicates that our Sensor Adapter approach can achieve an equivalent performance of the independent internal LiDAR clock while avoiding calculating the temporal offset between independent clock references for data alignment.

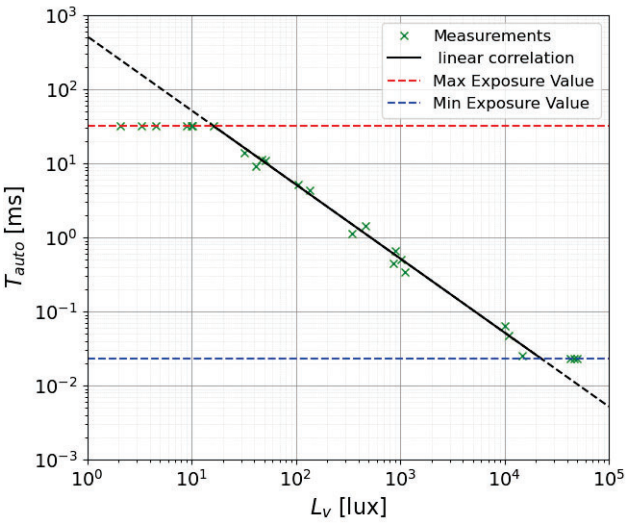

Fig. 8: Relationship between ambient light intensities L_v and corresponding automatic exposure durations T_{strobe}

B. Exposure duration & IMU sampling index identification

To find the target index $\lfloor n^* \rceil$ for eliminating the deviation d_{CI}, we need to obtain the automatic exposure duration T_{auto} first. Therefore, an external ambient light sensor was designed to identify the relationship (3) and measure the current light intensity L_v. A prototype of the ambient light sensor is shown in Fig. 2(b), which includes three independent ambient light chips to enable cross-sampling and

minimize the inherent latency associated with relying on a single chip for the sampling process. With this prototype, we collected a group of data and got their relationship in the camera exposure range as (8) through data fitting. The corresponding results are shown in Fig. 8. Substituting the current light intensity L_v into (8), we can get the current T_{auto}. Then, we can further obtain $\lfloor n^* \rceil$ by (6).

$$T_{auto} = f(L_v) = 520.31\, {L_v}^{-1}. \tag{8}$$

C. Evaluation of time deviation in Visual-Inertial system

We compared our method with existing approaches by setting the Visual-Inertial system working under three different synchronization methods:

1) Traditional method - trigger the camera periodically and poll data-reading requests to the IMU simultaneously.
2) VI-Sensor method - consider the exposure delay from the camera and poll data-reading request to the IMU simultaneously [18].
3) Our Sensor Adapter method - optimize the camera exposure duration and align its midpoint t_C to the authentic IMU sampling moment $t_I^{\lfloor n^* \rceil}$.

Then, we evaluated the effectiveness of these three synchronization methods using two time-offset assessment approaches: measuring the dynamic time offset by analyzing real-time data and estimating the constant time offset by using the well-known open-source calibration tool Kalibr [6]–[8]. Kalibr uses the camera and IMU to capture a sequence of calibration target images and IMU readings. After optimization processes, it outputs the estimated constant timestamp offset and the intrinsic and extrinsic parameters of the system.

1) Dynamic time offset evaluation: For each synchronization method, we collected datasets and signal waveforms from the logical analyzer at three exposure durations. The corresponding temporal offset histogram is shown in Fig. 9. Three methods had the lowest temporal offset at the first exposure duration. In the first duration, from Fig. 9, we can see that our approach had a lower time offset (0.0011ms) compared to that of the other two methods (0.6476ms and 0.0476ms). This indicates our method can effectively reduce the dynamic deviation d_{CI} in the Visual-Inertial system. The temporal offset variation indicated by the standard deviation value of our method (0.0003ms) was also significantly less than that of the V-I method (0.1934ms). Moreover, the temporal offset of two other methods kept increasing when the camera duration increased, while our method demonstrated consistent performance. These imply that our method is more robust and reliable.

2) Constant time offset evaluation: We used time-shift values from calibration results obtained with the well-known spatial and temporal calibration toolbox, Kalibr, to evaluate the effectiveness of different synchronization methods in the Visual-Inertial system. The time-shift value, calculated as a constant in calibration results, reflects better time synchronization performance when it is smaller. As listed in Table III, our proposed Sensor Adapter approach has

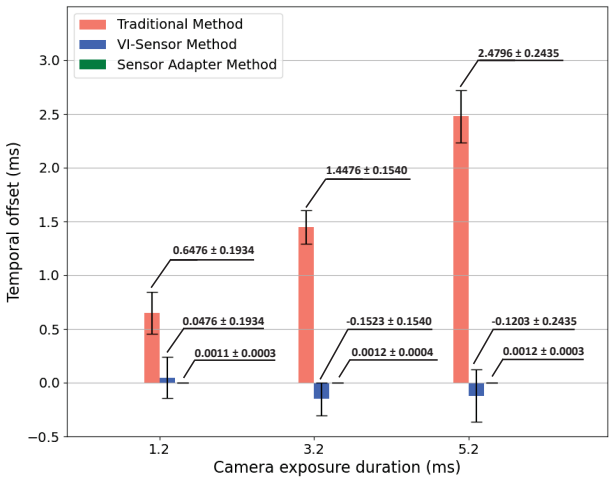

Fig. 9: Temporal offset comparison of three methods. The positive and native temporal offsets are described in (2) and Fig. 5.

Methods	Image Acquisition Mode	Time Offset [ms]
Tradition	Auto Exposure	20.0715
VI-Sensor	Auto Exposure	1.7714
Sensor Adapter	Bulb Shutter Mode	0.2255

TABLE III: Visual-Inertial system calibration results for three synchronization methods. In Bulb Shutter mode, the camera integrates the incoming light from the external trigger signal. Integration time equals the high state time of the external trigger signal.

the minimum constant time offset (0.2255ms) compared to the other two methods (20.0715ms and 1.7714ms). This further confirms that our Sensor Adapter approach can significantly reduce deviation d_{CI} in Visual-Inertial systems by considering both camera exposure and IMU sampling in the synchronization system.

V. Conclusion

In this study, we presented a novel hardware architecture to enable the precise synchronization of the LVI system or more sensors under a unified clock reference. We then proposed a hardware-based synchronization method that enables simultaneous sampling in the Visual-Inertial system. To evaluate the architecture design, we built a prototype and demonstrated that it can achieve time synchronization under a unified clock reference in the LVI system. Then, we compared our method with existing approaches in dynamic and constant time offset scenarios. The results demonstrate that our method can achieve higher precision time synchronization and be successfully implemented in multi-sensor systems. The proposed method can potentially help researchers practically reduce the time delays in the multi-sensor system and enhance its robustness and reliability.

In the future, we plan to implement our system in UAV light systems and further verify its feasibility in scenarios that require accurate time synchronization, such as simultaneous localization and mapping in a mine environment.

REFERENCES

[1] J. Sock, J. Kim, J. Min, and K. Kwak, "Probabilistic traversability map generation using 3d-lidar and camera," in *2016 IEEE international conference on robotics and automation (ICRA)*. IEEE, 2016, pp. 5631–5637.

[2] K. Eckenhoff, P. Geneva, and G. Huang, "Mimc-vins: A versatile and resilient multi-imu multi-camera visual-inertial navigation system," *IEEE Transactions on Robotics*, vol. 37, no. 5, pp. 1360–1380, 2021.

[3] H. Zhang, L. Du, S. Bao, J. Yuan, and S. Ma, "Lvio-fusion: Tightly-coupled lidar-visual-inertial odometry and mapping in degenerate environments," *IEEE Robotics and Automation Letters*, 2024.

[4] J. Kelly and G. S. Sukhatme, "A general framework for temporal calibration of multiple proprioceptive and exteroceptive sensors," in *Experimental Robotics: The 12th International Symposium on Experimental Robotics*. Springer, 2014, pp. 195–209.

[5] E. Mair, M. Fleps, M. Suppa, and D. Burschka, "Spatio-temporal initialization for imu to camera registration," in *2011 IEEE International Conference on Robotics and Biomimetics*. IEEE, 2011, pp. 557–564.

[6] P. Furgale, T. D. Barfoot, and G. Sibley, "Continuous-time batch estimation using temporal basis functions," in *2012 IEEE International Conference on Robotics and Automation*. IEEE, 2012, pp. 2088–2095.

[7] P. Furgale, J. Rehder, and R. Siegwart, "Unified temporal and spatial calibration for multi-sensor systems," in *2013 IEEE/RSJ International Conference on Intelligent Robots and Systems*. IEEE, 2013, pp. 1280–1286.

[8] J. Rehder, J. Nikolic, T. Schneider, T. Hinzmann, and R. Siegwart, "Extending kalibr: Calibrating the extrinsics of multiple imus and of individual axes," in *2016 IEEE International Conference on Robotics and Automation (ICRA)*. IEEE, 2016, pp. 4304–4311.

[9] T. Qin and S. Shen, "Online temporal calibration for monocular visual-inertial systems," in *2018 IEEE/RSJ International Conference on Intelligent Robots and Systems (IROS)*. IEEE, 2018, pp. 3662–3669.

[10] K. Qiu, T. Qin, J. Pan, S. Liu, and S. Shen, "Real-time temporal and rotational calibration of heterogeneous sensors using motion correlation analysis," *IEEE Transactions on Robotics*, vol. 37, no. 2, pp. 587–602, 2020.

[11] D. L. Mills, "Internet time synchronization: the network time protocol," *IEEE Transactions on communications*, vol. 39, no. 10, pp. 1482–1493, 1991.

[12] F. Tungadi and L. Kleeman, "Time synchronisation and calibration of odometry and range sensors for high-speed mobile robot mapping," in *Proc. Australasian Conference on Robotics and Automation*, 2008.

[13] A. Harrison and P. Newman, "Ticsync: Knowing when things happened," in *2011 IEEE International Conference on Robotics and Automation*. IEEE, 2011, pp. 356–363.

[14] E. Mueggler, G. Gallego, H. Rebecq, and D. Scaramuzza, "Continuous-time visual-inertial odometry for event cameras," *IEEE Transactions on Robotics*, vol. 34, no. 6, pp. 1425–1440, 2018.

[15] C. Sommer, V. Usenko, D. Schubert, N. Demmel, and D. Cremers, "Efficient derivative computation for cumulative b-splines on lie groups," in *Proceedings of the IEEE/CVF Conference on Computer Vision and Pattern Recognition*, 2020, pp. 11 148–11 156.

[16] C. Zheng, Q. Zhu, W. Xu, X. Liu, Q. Guo, and F. Zhang, "Fast-livo: Fast and tightly-coupled sparse-direct lidar-inertial-visual odometry," in *2022 IEEE/RSJ International Conference on Intelligent Robots and Systems (IROS)*. IEEE, 2022, pp. 4003–4009.

[17] V. Osadcuks, M. Pudzs, A. Zujevs, A. Pecka, and A. Ardavs, "Clock-based time synchronization for an event-based camera dataset acquisition platform," in *2020 IEEE International Conference on Robotics and Automation (ICRA)*. IEEE, 2020, pp. 4695–4701.

[18] J. Nikolic, J. Rehder, M. Burri, P. Gohl, S. Leutenegger, P. T. Furgale, and R. Siegwart, "A synchronized visual-inertial sensor system with fpga pre-processing for accurate real-time slam," in *2014 IEEE international conference on robotics and automation (ICRA)*. IEEE, 2014, pp. 431–437.

[19] W. Ding, J. Wang, Y. Li, P. Mumford, and C. Rizos, "Time synchronization error and calibration in integrated gps/ins systems," *ETRI journal*, vol. 30, no. 1, pp. 59–67, 2008.